Diffusion MRI simulation in thin-layer and thin-tube media using a discretization on manifolds

Van-Dang Nguyen [a,*], Johan Jansson [a], Hoang Trong An Tran [b], Johan Hoffman [a], Jing-Rebecca Li [b]

[a] *Department of Computational Science and Technology, KTH Royal Institute of Technology, Sweden*
[b] *CMAP – Center for Applied Mathematics, Ecole Polytechnique, Palaiseau, France*

ARTICLE INFO

ABSTRACT

The Bloch-Torrey partial differential equation can be used to describe the evolution of the transverse magnetization of the imaged sample under the influence of diffusion-encoding magnetic field gradients inside the MRI scanner. The integral of the magnetization inside a voxel gives the simulated diffusion MRI signal. This paper proposes a finite element discretization on manifolds in order to efficiently simulate the diffusion MRI signal in domains that have a thin layer or a thin tube geometrical structure. The variable thickness of the three-dimensional domains is included in the weak formulation established on the manifolds. We conducted a numerical study of the proposed approach by simulating the diffusion MRI signals from the extracellular space (a thin layer medium) and from neurons (a thin tube medium), comparing the results with the reference signals obtained using a standard three-dimensional finite element discretization. We show good agreements between the simulated signals using our proposed method and the reference signals for a wide range of diffusion MRI parameters. The approximation becomes better as the diffusion time increases. The method helps to significantly reduce the required simulation time, computational memory, and difficulties associated with mesh generation, thus opening the possibilities to simulating complicated structures at low cost for a better understanding of diffusion MRI in the brain.

© 2019 Elsevier Inc. All rights reserved.

1. Introduction

Diffusion magnetic resonance imaging (dMRI) is a non-invasive technique that makes use of the diffusional process of water molecules to probe the micro-structure of biological tissues. After being discovered to be useful in detecting troke in its acute phase in 1990s [1,2], dMRI has been used to image almost every part of the human body. In the brain, the micro-structure is extraordinarily complicated: cells such as neurons and glials cells crowd together, leaving a tortuous extracellular space (ECS). Neurons are made of a central body (soma) to which are attached long protrusions called neurites (axons and dendrites), the axons being long cylinders and the dendrites having a tree structure. In a neuron, the diameter of the soma is on the order of 10 μm, the diameter of the dendrite segments can range from a few micrometers to less than half a micrometer, and the total length of all the dendrite segments is on the order of several millimeters [3,4]. Fig. 1a shows the morphology of dendritic trees reproduced from [5]. The neuron on the top left from the drosophila melanogaster has 123 dendrite

branches with the average diameter of 1 μm. The human neuron on the right has 585 dendrite branches and the average diameter of 0.3 μm. The two neurons have soma surface areas of 3.14 μm² and 693.5 μm², respectively. The ECS is the space outside of the cells (such as neurons and glial cells) that has a complicated geometrical structure because the cells are irregularly shaped and packed tightly together. A recent study indicates that the average thickness of the ECS in the *in vivo* rat cortex is between 38 and 64 nm (see the review [6] and citations therein). In Fig. 1b we show the extracellular space (marked in red) of a small region of the rat cortex [6–8].

The extraction of quantitative micro-structure information from dMRI measurements has sustained a vast amount of research. By simulating individual structures such as neurons and the extracellular space, one hopes to build up a model of the dMRI signal at the voxel or the region-of-interest level that combines these individual structures. Water exchange between the structures through cell membranes can be added to the basic model later.

The predominant approach up to now has been building the dMRI signal from simple geometrical components and models: (1) analytical diffusion models in cylinders, spheres, etc.; (2) Gaussian diffusion tensor in extra-cellular space; and then extracting the model parameters: volume fraction and size distribution of

* Corresponding author.
E-mail addresses: vdnguyen@kth.se (V.-D. Nguyen), jjan@kth.se (J. Jansson), jhoffman@kth.se (J. Hoffman), jingrebecca.li@inria.fr (J.-R. Li).

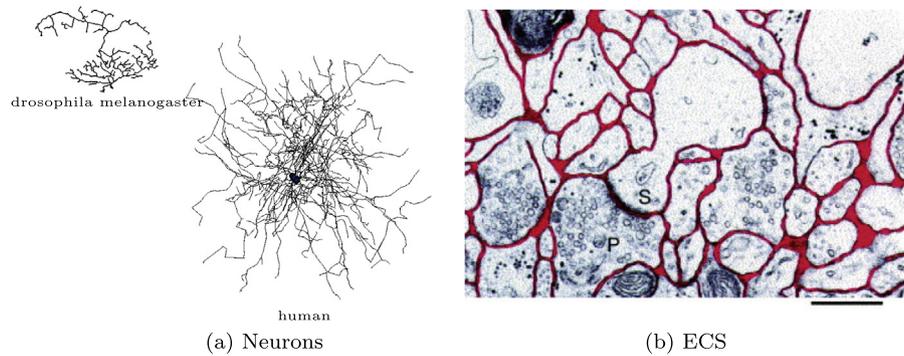(a) Neurons   (b) ECS

Fig. 1. (a) Morphology of dendritic trees reproduced from [5]. The neuron on the left from the drosophila melanogaster has 123 dendrite branches and the average diameter of 1 μm. The human neuron on the right has 585 dendrite branches and the average diameter of 0.3 μm. The two neurons have soma surface areas of 3.14 μm^2 and 693.5 μm^2, respectively. (b) The extracellular space (marked in red) of a small region of the rat cortex with the scale bar of 1 μm. The image was reprinted from [7] with permission from Elsevier and Prof. Eva Syková. (For interpretation of the references to colour in this figure legend, the reader is referred to the web version of this article.)

cylinder and sphere components, intrinsic and effective diffusion coefficients and tensors [9–11]. To to deepen the understanding of the relationship between cellular structure and the dMRI signal in complicated geometries, one needs to rely on numerical simulations. In the same vein, improving the efficiency of dMRI simulations can accelerate the computational procedure in the estimation of model parameters and allows the use of more complicated geometrical components such as trees structures. Numerical simulations also provide a cheap and powerful tool to investigate the effect of different pulse sequences and tissue features on the measured signal which can be used for development, testing, and optimization of novel MRI pulse sequences [16,17].

Two main groups of approaches to the numerical simulation of dMRI are (1) using random walkers to mimic the diffusion process in a geometrical domain; (2) solving the Bloch-Torrey partial differential equation (PDE), which describes the evolution of the transverse water proton magnetization under the influence of diffusion-encoding magnetic field gradients pulses. The first group is referred to as Monte-Carlo simulations in the literature and previous works include [18–20,13]. A GPU-based acceleration of Monte-Carlo simulation was proposed in [21]. The second group of simulations rely on solving the Bloch-Torrey PDE in a geometrical domain, either using finite difference methods (FDM) [22–25], typically on a Cartesian grid, or finite element methods (FEM), typically on a tetrahedral grid. For previous work on FEM, it is recommended to refer to [26] for the short gradient pulse limit of some simple geometries, to [27] for the multi-compartment Bloch-Torrey equation with general gradient pulses, and to [28] with the flow and relaxation terms added. In [29], a simplified 1D manifold Bloch-Torrey equation was solved to study the dMRI signal from neuronal dendrite trees. A high performance FEM computing framework was proposed in [30,31] for large-scale dMRI simulations on supercomputers. A comparison of the Monte-Carlo approach with the FEM approach is beyond the scope of this paper. Such a comparison for the short pulse limit was done in [26], where FEM simulations were evaluated to be much more accurate and faster than the equivalent modeling with Monte-Carlo simulations.

Based on the numerical simulations, a study in [12] shows the effect of neuronal dendrite tree structures to the dMRI signal in brain tissue. More recently, complicated components have been used for diffusion-weighted MR spectroscopy (using several metabolites), with neurons and astrocytes being represented by one-dimensional tree structures [13]. The model parameters in this case were the mean values and the standard deviations of branch lengths and branch numbers, as well as the intrinsic diffusion coefficient. The use of one-dimensional components in that study was justified by the long diffusion times (from 52 ms up to 2002 ms).

The extraction of morphological properties of two different types of neurons was preliminarily evoked in [14]. Similarly, studying the diffusion characteristics of the extracellular space can reveal information about its structure, and models are emerging based on MRI [15,7].

The focus of this paper is the simulation of dMRI signals in thin structures, which is usually memory-demanding and time-consuming. For Monte-Carlo approaches, if the reflection condition is applied, the particle undergoes multiple reflections until no further surface intersections are detected [20,21], and if the rejection method [32] is applied, the time step sizes need to be small to be accurate. This process becomes extremely time-consuming if the layer is thin. Similarly for FEM and FDM, because of the thin geometrical structures of the neurons and the ECS, it requires tiny elements or grid sizes to describe the geometry correctly and at the same time maintain the mesh quality. A naive mesh generator would generate an excessively large number of elements. The time step sizes also need to be small to ensure the accuracy and stability of the methods.

Based on the fact that the radius of the dendrites and the thickness of the ECS are much smaller than the diffusion displacement of interest, it is commonly accepted that the diffusion in the 'thin' direction quickly reaches steady-state, whereas the interesting physics occurs in a lower dimensional manifold perpendicular to the 'thin' direction. Therefore, the topological dimension of the computational domain can be reduced to make MRI simulations more efficient. The work in this paper is related to an approach developed in [29] to model dendrite trees as one-dimensional linked segments, where the neurite thickness is assumed to be constant in the entire tree. The interaction of the one dimensional tree structure with the three-dimensional soma was also included, and a study of the diffusion MRI signal for such domains was made [12]. In this paper, variable segment diameters are included into the formulation for dendrite trees, and this approach is extended to the ECS of variable thickness. An underlying lower dimensional manifold is assumed in one dimension for the dendrite tree and in two dimensions for the ECS. These manifolds are approximated by a surface triangulation (union of straight segments for dendrite trees and union of flat panels for the ECS). The discretization is formulated on the surface triangulation nodes. The Cartesian Laplacian operator is projected onto the surface triangulation, and the unknown magnetization is multiplied by a factor that is the layer thickness for the ECS and the cross section area for the dendrite tree. A numerical study is conducted to compare the simulated diffusion MRI signals using the proposed method with reference signals computed using standard three-dimensional volume finite elements.

The proposed method was implemented with the open source software FEniCS [33,34], which was started in 2003 to realize the vision of efficiently solving PDEs by FEM with a high-level mathematical notation. Formulating FEM on lower-dimensional manifolds is today possible in FEniCS either through a direct extension of the framework to manifolds [35], or by a CutFEM approach [36]. The direct approach is chosen since the generality of CutFEM is not needed. The FEniCS framework allows for the automated solution of many classes of PDEs of key societal and academic importance. FEniCS opens the way for an automated approach since it provides rapid development and efficient implementation, as well as a framework for reliable control of errors in the solution. The reliability is especially critical in medical applications.

The paper is organized as follows. First, in Section 2 we present the Bloch-Torrey PDE and propose a numerical solution that consists of a space discretization on a surface triangulation and review the θ−method as the time discretization. We describe the implementation of the proposed method on the FEniCS platform in Section 3 where the equation is decomposed into two sub-equations, for the real and imaginary parts. Then we give details about the numerical simulations in Section 4, including information about the meshes and the dMRI parameters. In Section 5, we present numerical results, showing the reliability of the numerical solutions as well as good agreements between the proposed approach and reference solutions. In Section 6 we discuss the fact that the proposed method approaches the reference solution as diffusion time increases, resulting in a drastic reduction in the computational time. Finally, in Section 7, we provide conclusions and propose future developments.

2. Theory

2.1. The Bloch-Torrey equation

The complex transverse water proton magnetization u in a three-dimensional domain Ω can be modeled by the Bloch-Torrey PDE [37]:

$$\frac{\partial u(\mathbf{x},t)}{\partial t} + i\gamma G(\mathbf{x})f(t)u(\mathbf{x},t) - \nabla \cdot (D\nabla u(\mathbf{x},t)) = 0, \quad \mathbf{x} \in \Omega \quad (1)$$

where i is the imaginary unit ($i^2 = -1$), D is the intrinsic diffusion coefficient, $G(\mathbf{x}) = \mathbf{g} \cdot \mathbf{x}, \mathbf{g}$ contains the amplitude and direction information of the applied diffusion-encoding magnetic field gradient, $\gamma = 2.67513 \times 10^8$ rad s^{-1} T^{-1} denotes the gyro-magnetic ratio of water proton, and $f(t)$ indicates the time profile of the diffusion-encoding magnetic field gradient sequence.

The most commonly used time profiles $f(t)$ to encode the diffusion include the pulsed-gradient spin echo sequence (PGSE) sequence [38] and the oscillating gradient spin echo (OGSE)

sequence [39]. The PGSE consists of two rectangular pulses of duration δ, separated by a time interval $\Delta - \delta$ (Fig. 2a):

$$f(t) = \begin{cases} 1, & 0 \leqslant t \leqslant \delta, \\ -1, & \Delta < t \leqslant \Delta + \delta, \\ 0, & \text{otherwise}. \end{cases} \quad (2)$$

The OGSE consists of two oscillating pulses of duration σ, each containing n periods, separated by a time interval $\tau - \sigma$ (Fig. 2b). For a cosine OGSE [40,39], the profile $f(t)$ is

$$f(t) = \begin{cases} \cos(n\frac{2\pi}{\sigma}t), & 0 < t \leqslant \sigma, \\ -\cos(n\frac{2\pi}{\sigma}(t-\tau)), & \tau < t \leqslant \tau + \sigma, \\ 0, & \text{otherwise}. \end{cases} \quad (3)$$

In this paper, the water exchange between compartments is neglected, yielding the homogeneous Neumann boundary condition:

$$D\nabla u(\mathbf{x},t) \cdot \mathbf{n} = 0, \quad \mathbf{x} \in \partial\Omega. \quad (4)$$

where $\mathbf{n}$ is the unitary normal vector pointing outward the boundary. Assuming a uniform excitation of the magnetization in the imaging voxel, the initial condition is $u(\mathbf{x}, 0) = 1$. The signal is measured at the echo time, TE, with $TE > \delta + \Delta$ for the PGSE and $TE > \sigma + \tau$ for the OGSE. The diffusion MRI signal is the total magnetization averaged over the computational domain Ω:

$$S(\mathbf{g}) = \frac{1}{|\Omega|} \int_\Omega u(\mathbf{x}, TE)\, d\mathbf{x}. \quad (5)$$

The signal is usually plotted against a quantity called the b−value. For the PGSE, the b-value is [38]:

$$b(\mathbf{g}, \delta, \Delta) = \gamma^2 \|\mathbf{g}\|^2 \delta^2 \left(\Delta - \frac{\delta}{3}\right). \quad (6)$$

For the cosine OGSE with the number of periods n in each of the two durations σ, the corresponding b-value is [23]:

$$b(\mathbf{g}, \sigma) = \gamma^2 \|\mathbf{g}\|^2 \frac{\sigma^3}{4n^2\pi^2}. \quad (7)$$

It is commonly agreed that a reasonable choice for the effective diffusion time, t_D, of the PGSE sequence is:

$$t_D = \Delta - \frac{\delta}{3},$$

and for cosine OGSE it is [39]:

$$t_D = \frac{\sigma}{4n}.$$

The unhindered mean squared displacement in three-dimensions is
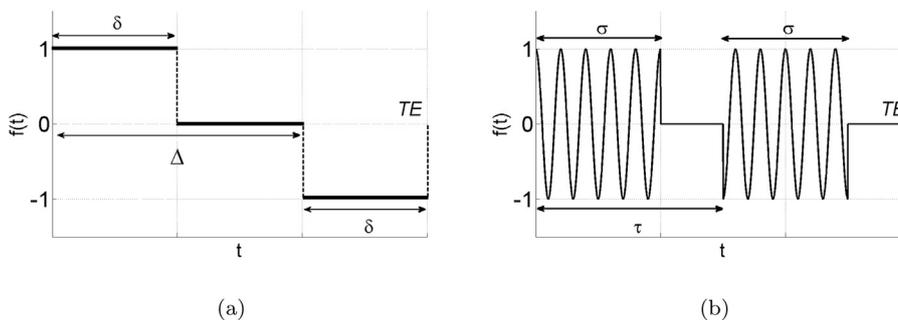
$$\text{MSD} = \sqrt{6Dt_D}.$$

Fig. 2. A PGSE sequence (a) and a cos-OGSE sequence (b).

In the next section, a finite element discretization on manifolds is derived in order to simulate the diffusion MRI signal in a thin layer or in a thin tube structure.

2.2. FEM formulation: from volumes to manifolds

The three-dimensional domain of simulation, $\Omega \subset \mathbb{R}^3$, is assumed to be described by a lower dimensional manifold Γ (of dimension two in the case of the ECS, of dimension one in the case of the dendrite tree) and a variable cross section $\mathcal{V}$, in other words:

$$\Omega = \left\{ (\widetilde{\boldsymbol{x}} + \widehat{\boldsymbol{x}}), \widetilde{\boldsymbol{x}} \in \Gamma, \ \widehat{\boldsymbol{x}} \in \mathcal{V}(\widetilde{\boldsymbol{x}}) \right\}.$$

In the case of ECS,

$$\Gamma \subset \mathbb{R}^2, \mathcal{V}(\widetilde{\boldsymbol{x}}) \subset \mathbb{R}^1$$

whereas in the case of dendrite trees,

$$\Gamma \subset \mathbb{R}^1, \mathcal{V}(\widetilde{\boldsymbol{x}}) \subset \mathbb{R}^2.$$

Let $\boldsymbol{Q} = \boldsymbol{H}^1(\Omega)$ be a Sobolev space, i.e.

$$\boldsymbol{H}^1(\Omega) = \left\{ v : \Omega \to \mathbb{C} \mid \int_\Omega v^2 + |\nabla v|^2 \, dx < \infty \right\}.$$

To construct the weak form of Eq. (1) we multiply both sides with a test function $v \in \boldsymbol{Q}$ and integrate over Ω, we then have

$$\int_\Omega \dot{u} \, v \, d\Omega = -\int_\Omega i\gamma f(t) \boldsymbol{G}(\boldsymbol{x}) u \, v \, d\Omega + \int_\Omega \nabla \cdot (D \nabla u) \, v \, d\Omega.$$

After applying the Green's first identity to the diffusion term, we obtain

$$\int_\Omega \dot{u} \, v \, d\Omega = -\int_\Omega i\gamma f(t) \boldsymbol{G}(\boldsymbol{x}) u \, v \, d\Omega + \int_{\partial\Omega} D \nabla u \cdot \boldsymbol{n} \, v \, ds - \int_\Omega D \nabla u \cdot \nabla v \, d\Omega.$$

The homogeneous Neumann boundary conditions (Eq. (4)) on $\partial\Omega$ cancel out the boundary term and give

$$\int_\Omega \dot{u} \, v \, d\Omega = -\int_\Omega i\gamma f(t) \boldsymbol{G}(\boldsymbol{x}) u \, v \, d\Omega - \int_\Omega D \nabla u \cdot \nabla v \, d\Omega. \tag{8}$$

We denote the surface triangulation of Γ by $\mathcal{T} = \bigcup_i \overline{E}_i$. Assume we have available the cross-section $\mathcal{V}(\widetilde{\boldsymbol{x}})$ at each node $\widetilde{\boldsymbol{x}}$ of $\mathcal{T}$. Specifically, for the ECS, let $\widetilde{\boldsymbol{x}}_1, \widetilde{\boldsymbol{x}}_2, \widetilde{\boldsymbol{x}}_3$ be the three nodes of the triangle $\overline{E}_i$, then the six points:

$$\left\{ \widetilde{\boldsymbol{x}}_1 + \alpha_1 \boldsymbol{n}(\widetilde{\boldsymbol{x}}_1), \quad \widetilde{\boldsymbol{x}}_2 + \alpha_2 \boldsymbol{n}(\widetilde{\boldsymbol{x}}_2), \quad \widetilde{\boldsymbol{x}}_3 + \alpha_3 \boldsymbol{n}(\widetilde{\boldsymbol{x}}_3) \right\}$$

where $\boldsymbol{n}(\widetilde{\boldsymbol{x}}_j), j = 1, 2, 3$ is perpendicular to Γ at $\widetilde{\boldsymbol{x}}_j$, and

$$\alpha_1 \in [a_1, b_1], \quad \alpha_2 \in [a_2, b_2], \quad \alpha_3 \in [a_3, b_3], \quad [a_k, b_k] \subset \mathbb{R}$$

make up the volume element E_i. In Fig. 3 we show the typical finite element for the ECS (Fig. 3b) and the dendrite tree (Fig. 3a).

Since our main interest is in performing diffusion simulations where the diffusion distance is large compared to the size of $\mathcal{V}$, we choose to enforce the following constraints on the solution:

$$u(\widetilde{\boldsymbol{x}} + \widehat{\boldsymbol{x}}) = u(\widetilde{\boldsymbol{x}}), \quad \widetilde{\boldsymbol{x}} \in \mathcal{T}, \quad \widetilde{\boldsymbol{x}} + \widehat{\boldsymbol{x}} \in \Omega. \tag{9}$$

In other words, the solution is constant on $\mathcal{V}(\widetilde{\boldsymbol{x}})$. Using the above constraint, we can simply solve for the values of the FEM solution at $\widetilde{\boldsymbol{x}} \in \mathcal{T}$.

We choose a continuous Galerkin discretization $\boldsymbol{Q}_h$ associated with a volume mesh of N nodes $\{\boldsymbol{x}_k\}_{k=1...N}$ and use standard basis functions $\{\varphi_k\}_{k=1...N}$ to give rise to the following representations:

$$u_h = \sum_{k=1}^N U_k \varphi_k, \quad G_h u_h = \sum_{k=1}^N G_k^h U_k \varphi_k. \tag{10}$$

where U_k and G_k^h are discretized values of u_h and G_h at the mesh node $\boldsymbol{x}_k$.

On each element $E \in \Omega_h$, Eq. (8) becomes

$$\int_E \dot{u}_h \, v_h \, dE = -\int_E i\gamma f(t) G_h u_h \, v_h \, dE + \int_{\partial E \partial \Omega} D \nabla u_h \cdot \boldsymbol{n} \, v_h \, ds$$
$$- \int_E D \nabla u_h \cdot \nabla v_h \, dE. \tag{11}$$

Note that the boundary term is automatically canceled due to the flux conservation

$$\sum_{E'} \int_{\partial E' \partial \Omega} D \nabla u_h \cdot \boldsymbol{n} \, v_h \, ds = 0, \tag{12}$$

here E' indicates the elements sharing the same boundary ∂E.

Choose $v_h = \varphi_j, j = 1 \ldots N$ and substitute Eq. (10) to Eq. (11), we obtain the following discrete equation

$$\sum_{k=1}^N \left(\dot{U}_k \int_E \varphi_k \varphi_j \, dE + i\gamma f(t) G_k^h U_k \int_E \varphi_k \varphi_j \, dE + D U_k \int_E \nabla \varphi_k \cdot \nabla \varphi_j \, dE \right) = 0. \tag{13}$$

Since $\{\varphi_k\}$ is defined on $\mathcal{T}$, the integral on E is decomposed and Eq. (13) becomes

$$\sum_{k=1}^N \left(\dot{U}_k \int_{\overline{E}} \varphi_k \varphi_j \eta_k \, d\overline{E} + i\gamma f(t) G_k^h U_k \int_{\overline{E}} \varphi_k \varphi_j \eta_k \, d\overline{E} \right.$$
$$\left. + D U_k \int_{\overline{E}} \nabla_{\overline{E}} \varphi_k \cdot \nabla_{\overline{E}} \varphi_j \eta_k \, d\overline{E} \right) = 0 \tag{14}$$
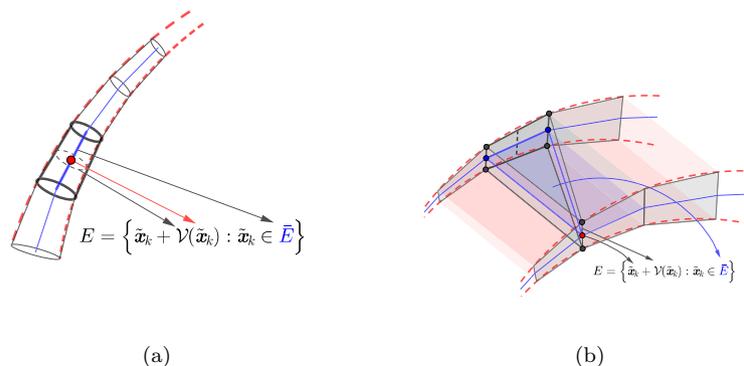

(a)   (b)

Fig. 3. In case the element is a tapered cylinder, the basis functions are defined on the edge $\overline{E}$ connecting two center points of circular bases (a). In case the element is a triangle prism, the basis functions are defined on the triangle $\overline{E}$ formed by midpoints of edges perpendicular to the middle surface (b).

where η_k is the cross-section area $\eta_k = |\mathcal{V}(\mathbf{x}_k)|$ and $\nabla_{\bar{E}}$ denotes the projection of the gradient operator on $\bar{E}$. For simplicity, from now on we use ∇ to denote $\nabla_{\bar{E}}$.

Let $\eta(\mathbf{x}) = |\mathcal{V}(\mathbf{x})|$ be the continuous function of the thickness and $\bar{E}'$ indicate the elements sharing the same boundary $\partial\bar{E}$, the flux conservation Eq. (12) becomes

$$\sum_{\bar{E}'} \int_{\partial\bar{E}'} D\nabla u_h \cdot \mathbf{n}\, v\, \eta\, ds = 0 \qquad (15)$$

which is implicitly imposed through the implementation of Eq. (14). Eq. (5) now becomes

$$S_m(\mathbf{g}) = \left(\int_\Gamma \eta(\mathbf{x})\, d\Gamma \right)^{-1} \int_\Gamma u_h(TE)\, \eta(\mathbf{x})\, d\Gamma. \qquad (16)$$

In case η is constant, Eq. (16) is simplified to [29]

$$S_m(\mathbf{g}) = \frac{1}{|\Gamma|} \int_\Gamma u_h(TE)\, d\Gamma. \qquad (17)$$

We also note that Eq. (14) allows solving the equation on surface meshes and the thickness is added to the equation analytically. The space–time discretization of Eq. (14) with the θ−method (used also in [28,31]) reads

$$\sum_{k=1}^N \left(\frac{U_k^{n+1} - U_k^n}{\Delta t} \int_{\bar{E}} \varphi_k\, \varphi_j\, \eta_k\, d\bar{E} + i\gamma\, G_k^h\, \mathcal{F}\left(U_k^{n+\theta}\right) \right.$$
$$\left. \times \int_{\bar{E}} \varphi_k\, \varphi_j\, \eta_k\, d\bar{E} + D U_k^{n+\theta} \int_{\bar{E}} \nabla\varphi_k \cdot \nabla\varphi_j\, \eta_k\, d\bar{E} \right) = 0 \qquad (18)$$

where $\theta \in [0,1], \Delta t = t^{n+1} - t^n$, and

$$U_k^{n+\theta} = \theta\, U_k^{n+1} + (1-\theta)\, U_k^n,$$

$$\mathcal{F}\left(U_k^{n+\theta}\right) = \theta f(t^{n+1})\, U_k^{n+1} + (1-\theta)f(t^n)\, U_k^n.$$

The explicit Forward Euler and implicit Backward Euler methods correspond to $\theta = 0$ and $\theta = 1$. Here, we use $\theta = \frac{1}{2}$ to have an implicit, unconditionally stable, and second-order method referred to as a Crank-Nicolson method. We will describe the detailed implementation in FEniCS in the next Section.

3. Implementation

FEniCS does not officially support complex-valued PDEs although this problem is under development [41]. So, to implement the proposed method in the current versions of FEniCS, we need to first decompose Eq. (18) into two equations for the real part and imaginary part. Then, we couple the two equations again into the linear and bilinear forms. For simplicity, we can write Eq. (18) as the following

$$\int_{\bar{E}} \frac{u_h^{n+1} - u_h^n}{\Delta t}\, v\eta\, d\bar{E} + i\gamma \int_{\bar{E}} G\mathcal{F}\left(u_h^{n+\theta}\right) v\eta\, d\bar{E} + D \int_{\bar{E}} \nabla u_h^{n+\theta} \cdot \nabla v\eta\, d\bar{E} = 0. \qquad (19)$$

Since u_h^n is complex-valued, we can write $u_h^n = u_h^{n,r} + i u_h^{n,i}$ and decompose Eq. (19) into two equations

$$\int_{\bar{E}} \frac{u_h^{n+1,r} - u_h^{n,r}}{\Delta t}\, v^r \eta\, d\bar{E} - \gamma \int_{\bar{E}} G\mathcal{F}\left(u_h^{n+\theta,i}\right) v^r \eta\, d\bar{E} + D \int_{\bar{E}} \nabla u_h^{n+\theta,r} \cdot \nabla v^r \eta\, d\bar{E} = 0,$$
$$\int_{\bar{E}} \frac{u_h^{n+1,i} - u_h^{n,i}}{\Delta t}\, v^i \eta\, d\bar{E} + \gamma \int_{\bar{E}} G\mathcal{F}\left(u_h^{n+\theta,r}\right) v^i \eta\, d\bar{E} + D \int_{\bar{E}} \nabla u_h^{n+\theta,i} \cdot \nabla v^i \eta\, d\bar{E} = 0. \qquad (20)$$

We choose to test the first equation with $v = v^r$ and the second equation with $v = v^i$.

The linear and bilinear forms corresponding to Eq. (20) are defined as

$$\mathbf{a}(u_h^{n+1}, v) = \frac{1}{\Delta t}\left(\int_{\bar{E}} u_h^{n+1,r}\, v^r \eta\, d\bar{E} + \int_{\bar{E}} u_h^{n+1,i}\, v^i \eta\, d\bar{E} \right) - \theta F(t^{n+1}, u_h^{n+1}),$$
$$\mathbf{L}(v) = \frac{1}{\Delta t}\left(\int_{\bar{E}} u_h^{n,r}\, v^r \eta\, d\bar{E} + \int_{\bar{E}} u_h^{n,i}\, v^i \eta\, d\bar{E} \right) + (1-\theta)F(t^n, u_h^n) \qquad (21)$$

where

$$F(t^n, u_h^n) = \gamma f(t^n) \int_{\bar{E}} G u_h^{n,i}\, v^r \eta\, d\bar{E} - D \int_{\bar{E}} \nabla u_h^{n,r} \cdot \nabla v^r \eta\, d\bar{E}$$
$$- \gamma f(t^n) \int_{\bar{E}} G u_h^{n,r}\, v^i \eta\, d\bar{E} - D \int_{\bar{E}} \nabla u_h^{n,i} \cdot \nabla v^i \eta\, d\bar{E}.$$

Eq. (21) was implemented in FEniCS C++ and Python as shown in the A. In the next section, we will describe the numerical study of the proposed method.

4. Numerical study

We conduct a numerical study of the proposed approach by simulating the diffusion MRI signal of thin tube and thin layer domains. The three methods to be compared are:

1. *Reference solution* (Method 1), the standard three-dimensional finite element discretization, with tetrahedral elements [31].
2. *Proposed method* (Method 2), the formulation on manifolds taking into account variable cross-section, as described in this paper.
3. *Previous method* (Method 3), the formulation on manifolds with a uniform cross-section [29]. In other words, $\eta_k = \bar{\eta}, \forall k$ in Eq. (14), where $\bar{\eta}$ is the averaged value.

4.1. Simulated domains

The simulation geometries are the following:

1. *Tree*, see Fig. 4.
   The 3D tree has variable cross-section. Each branch is modeled as a tapered cylinder with two different radii: r_1 and r_2. Here $r_1 = \{2, 1, 0.5\}\,\mu m$ and $r_2 = \{1, 0.5, 0.2\}\,\mu m$ correspond to three generations of the tree. The total length is 1211 μm.
2. *Neuron*, see Fig. 5a.
   The 3D neuron is from the drosophila melanogaster [5,42], with the average dendrite diameter being 1 μm, total length being 2462 μm. The 1D neuron is manually generated by connecting the centers of the cross-sections of the dendrite segments of the 3D neuron.
3. *Thick Plane*, see Fig. 5b.
   The thickness varies between 0.5 μm and 4 μm. Analytically, the thickness is expressed as $\eta(x,y,z) = \frac{9}{4} - \frac{x}{10} - \frac{z}{50}$. The corresponding 2D plane is $ABCD$ with $A(12.5; 0; 25)$, $B(12.5; 0; -25), C(-12.5; 0; -25), D(-12.5; 0; 25)$.
4. *Model ECS* (extra-cellular space), see Fig. 6.
   This is made of random planes whose thickness varies between 0.3 μm and 0.9 μm. The thickness function η is shown on the corresponding 2D manifold domain in Fig. 6b.

4.2. Mesh generation

The surface meshes for the above geometries were generated either with Salome [43] or from a medical segmentation with ANSA [44]. To generate the volume finite element mesh, we wrapped the STL mesh and generated a watertight surface mesh from ANSA. The surface meshes of the Tree, the Thick Plane and the Model ECS were generated from manually defined geometries
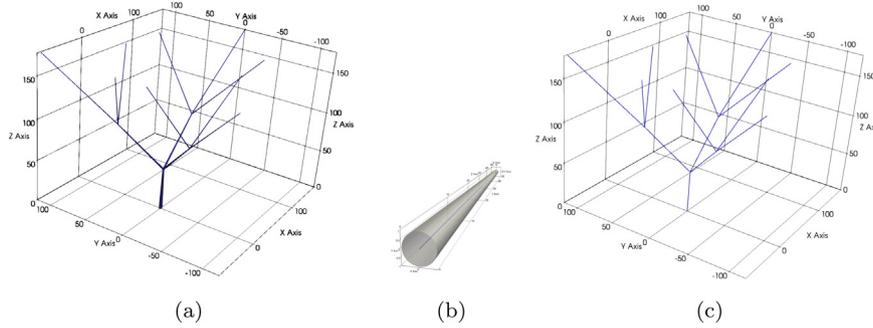
Fig. 4. A tree with variable cross-sections (a). Each branch is modeled as a tapered cylinder with two different radii r_1 and r_2 (b). Here $r_1 = \{2, 1, 0.5\}$ μm and $r_2 = \{1, 0.5, 0.2\}$ μm correspond to three generations of the tree. The corresponding 1D tree is shown in (c).
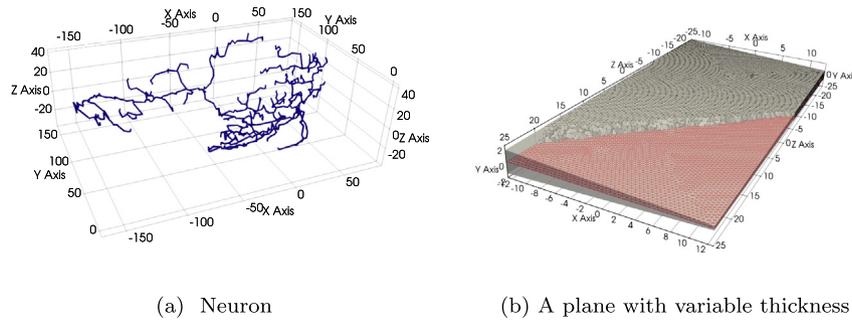

(a) Neuron

(b) A plane with variable thickness

Fig. 5. 3D neuron (a). A thick plane with variable thickness $\eta(x, y, z) = 9/4 - x/10 - z/50$ (b).

(a) 3D ECS

(b) 2D ECS

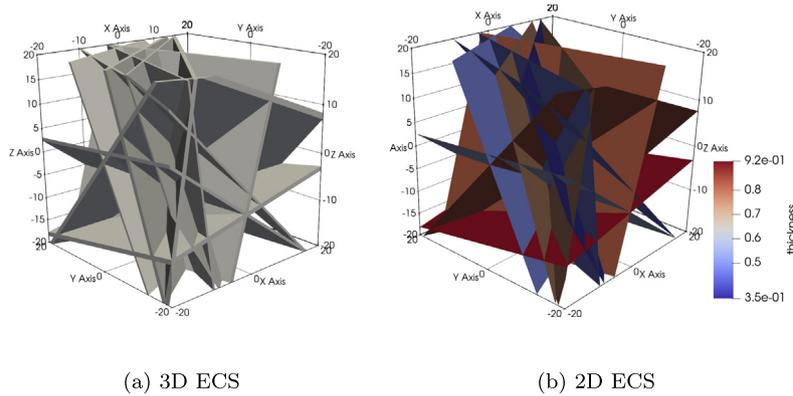**Fig. 6.** An artificial ECS made of random planes whose thickness varies between 0.3 μm and 0.9 μm (a). The function of thickness η is shown on the corresponding 2D manifold (b).

with the help of `Boolean Operations` in Salome in which we need to remove some gaps and intersections. For the Neuron, we downloaded the morphology file `fru-M-100383.swc` from the website [5,42]. It was then converted to the STL file format.

In Section 2.2, we idealized the thin domains as one layer of special elements along a manifold to establish the formulas. However, it is not practical to generate a volume finite element mesh consisting of one layer of elements, at least not in a robust way with existing finite element meshing resources. Therefore, the standard finite element meshes used to generate reference signals in the next section have elements that are much smaller than the thickness of the thin layers.

Table 1 shows the size of the volume and manifold meshes used for numerical simulations, corresponding to the above described domains. The thickness of the 3D tree varies significantly: between 0.2 and 2 μm. This kind of domain needs to be meshed with a large number of tetrahedra and it is the most expensive.

4.3. DMRI parameters

In the following, we will use the following format to describe the dMRI parameters of the simulations:

$$\begin{cases} \text{PGSE}(\delta, \Delta) \\ \text{OGSE}(\sigma = \tau) \end{cases}, \quad \boldsymbol{u}_g \equiv \frac{\boldsymbol{g}}{\|\boldsymbol{g}\|}, \quad b,$$

where for the OGSE sequence, we always use the cosine OGSE with $n = 2$ and $\sigma = \tau$. The time unit is (ms) and the b unit is (s/mm^2).

4.3.1. B-value

We simulated b−values between 0 and 4000 s/mm^2 which contain the feasible range of the vast majority of existing MRI scanners [45–47].

Table 1
Information about the volume and manifold meshes corresponding to the geometries on which numerical simulations were performed. The length unit is (μm).

Sample	Thickness	h_{min}	h_{max}	h_{mean}	# vertices	# elements
Tree 1D	0.2–2	0.5	0.5	0.5	1216	1215
Tree 3D		0.03	0.5	0.08	761175	3411547
Neuron 1D	1	0.4	1.9	0.9	1335	1342
Neuron 3D		0.03	0.9	0.3	65260	199973
Plane 2D	0.5–4	0.2	0.4	0.3	5869	11436
Plane 3D		0.2	0.8	0.4	24379	103595
Model ECS 2D	0.3–0.9	0.08	0.9	0.6	21986	46336
Model ECS 3D		0.004	6.0	0.4	87580	293792

4.3.2. Diffusion time

The effective diffusion time t_D varies for different applications but can be between 0.38 and 40 ms for the OGSE (see a review in [48]). For a PGSE, t_D is larger and can be up to ~1 s [13]. In this paper, t_D is varied between 5 and 500 ms for the PGSE and between 1.3 ms and 6.3 ms for the OGSE.

4.3.3. Gradient directions

At the most complicated, the simulations were performed over a set $\mathcal{G}$ of 270 gradients, quasi-uniformly distributed on a sphere (as used in [14]). The distribution of the three corresponding b−values, $1000, 2000$, and $3000 \, \text{s/mm}^2$, over the 270 gradient directions in that study is shown in Fig. 7. Here ϕ represents the horizontal azimuth angle measured on the xy−plane from the x−axis in the counterclockwise direction, and θ represents the azimuth angle measured from the z−axis in the spherical coordinates.

5. Results

The simulations on manifolds and small-scale volumes were performed with FEniCS 1.8.0 [34,31] on a stationary desktop (Intel(R) Core(TM) i7-3770 CPU@3.40 GHz) equipped with Linux Ubuntu 16.04 LTS, where timing comparisons were carried out. For large-scale volumes, the simulations were performed with FEniCS-HPC [49,30,31] on the KTH Beskow supercomputer [50] with 32 MPI proce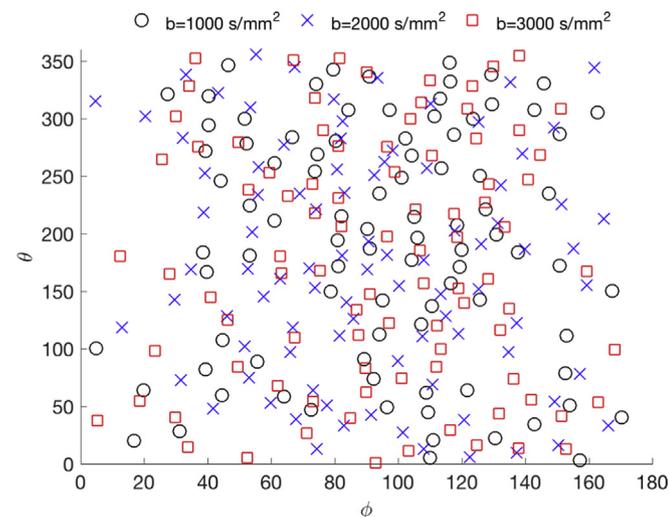sses for each b−value. A Krylov solver is used with the biconjugate gradient stabilized method and the block-Jacobi preconditioner from the PETSc library. The water diffusion coefficient used is $D = 3 \times 10^{-3} \, \text{mm}^2/\text{s}$.

The accuracy of our manifold model (Eq. (14)), compared to the full 3D model (Eq. (8)), is measured using the relative difference between the signals, computed by Eqs. (5) and (16), i.e.:

$$\mathcal{R} = \frac{|S(\boldsymbol{g}) - S_m(\boldsymbol{g})|}{S(\boldsymbol{g})}. \tag{22}$$

$\mathcal{R}_{max}$ and $\mathcal{R}_{mean}$ are used to indicate the maximum and the mean value of $\mathcal{R}$ over all gradient directions.

Before presenting the results of the simulations using the meshes described in Table 1, we check that the results are reliable by refining the spatial mesh and the time step of the Crank-Nicolson method. We generated refined meshes with a mean element size that is half of the original meshes; two Crank-Nicolson time steps, $\Delta t = 0.02$ ms and $\Delta t = 0.04$ ms, were used. The dMRI parameters were:

$$\text{PGSE}(10, 10), \quad \boldsymbol{u}_g = \frac{[1, 1, 1]}{\sqrt{3}}, \quad b = 4000 \, \text{s/mm}^2.$$

The computed signals for the Tree, the Neuron, and the Model ECS are shown in Table 2. The biggest change in the simulated signal is about 1.3% for Model ECS. Such small changes show that the numerical solution is stable and the meshes listed in Table 1 are adequate for comparing the proposed method and the reference solution. In addition, it can be seen in the table that the computation times on the manifolds are significantly smaller than on 3D domains. In particular, the 1D simulations take negligible time.

From now on, we fix the time step size to be $\Delta t = 0.04$ ms for all simulations in the following sections.

5.1. Tree

We first compare the signals of Methods 1, 2, and 3 for four PGSE sequences, with the following dMRI parameters:

$$\begin{cases} \text{PGSE}(1, 5), \\ \text{PGSE}(1, 10), \\ \text{PGSE}(1, 40), \\ \text{PGSE}(1, 200), \end{cases} \quad \boldsymbol{u}_g \in \mathcal{G}, \quad b \in \{1000, 2000, 3000\}.$$

The corresponding MSDs are $9.2 \, \mu m, 13.2 \, \mu m, 26 \, \mu m$ and $60 \, \mu m$. The results are shown in Fig. 8. The proposed method (Method 2) gives a good approximation to the reference model (Method 1) and the approximation gets better at longer diffusion times. The relative differences are 12.5%, 6.8%, 4.6% and 3.0%, respectively. The constant cross-Section 1D model (Method 3) gives a much worse approximation in this case with the relative differences being 120%, 100%, 56% and 37%, respectively.

Now we compare Method 1 and Method 2 for two cosine OGSE sequences (Eq. (3)). The following dMRI parameters were used:

Fig. 7. The distribution of b−values over the 270 gradient directions on a sphere, used in the numerical simulations. Here ϕ represents the horizontal azimuth angle measured on the xy−plane from the x−axis in the counterclockwise direction, and θ represents the azimuth angle measured from the z−axis in the spherical coordinates.

Table 2
The mesh sizes and the time-step size are reduced by half to observe the signals changes for $\delta = \Delta = 10$ ms and $b = 4000$ s/mm^2.

Sample	Original mesh ($\Delta t = 0.04$ ms)			Refined mesh ($\Delta t = 0.02$ ms)	
	signal	h_{mean}	Timing (s)	Signal	h_{mean}
Tree 1D	0.1883	0.50	1.0	0.1893	0.25
Tree 3D	0.2040	0.08	9897.0	0.2042	0.05
Neuron 1D	0.2551	0.90	1.0	0.2566	0.45
Neuron 3D	0.2521	0.30	812.5	0.2540	0.16
Model ECS 2D	0.0375	0.60	79.6	0.0381	0.28
Model ECS 3D	0.0352	0.40	1614.7	0.0357	0.26

(a) $\mathcal{R}_{max}$ verus Δ (b) Signals for a PGSE with $\Delta = 5$ ms
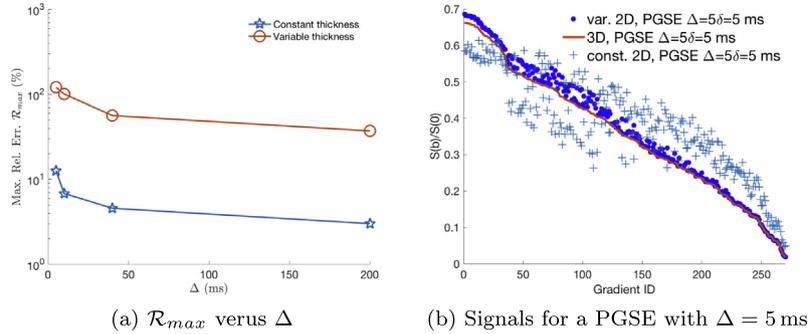
Fig. 8. A comparison of signals on the tree shown in Fig. 4 for four PGSE sequences with $\Delta = 5$ ms, $\Delta = 10$ ms, $\Delta = 40$ ms and $\Delta = 200$ ms (a). The variable cross-section model gives a good approximation to the 3D model and the approximation gets better at longer diffusion times. The relative differences are 12.5%, 6.8%, 4.6% and 3.0%, respectively. The constant cross-Section 1D model gives a much worse approximation in this case with the relative differences being 120%, 100%, 56% and 37%, respectively. Fig. (b) shows the signals at $\Delta = 5$ ms for which the relative difference is much smaller for Method 2 than for Method 3.

$$\begin{cases} \text{OGSE}(20) \\ \text{OGSE}(40) \end{cases} \boldsymbol{u}_g \in \mathcal{G}, \quad b \in \{1000, 2000, 3000\};$$

The relative difference is about 15.5% at $\sigma = \tau = 20$ ms. Similarly, the approximation gets better at longer diffusion time and the relative error is less than 5% at $\sigma = \tau = 40$ ms (Fig. 9).

5.2. Neuron

Now we consider the Neuron and compare Method 1 and Method 2 for three cosine OGSE sequences (Eq. (3)). The following dMRI parameters were used:

$$\begin{cases} \text{OGSE}(10) \\ \text{OGSE}(30) \, \boldsymbol{u}_g \in \mathcal{G}, \quad b \in \{1000, 2000, 3000\}; \\ \text{OGSE}(50) \end{cases}$$

The results are shown in Figs. 10a and b in which the relative difference is less than 17% for all gradient directions and the mean relative difference is around 4%. Again, the approximation gets bet-

ter at longer diffusion time and the maximum of the relative difference drops to 7% for $\sigma = \tau = 30$ ms.

Simulations were also performed with the following PGSE sequences:

$$\begin{cases} \text{PGSE}(5, 10), \\ \text{PGSE}(20, 80), \, \boldsymbol{u}_g \in \mathcal{G}, \quad b \in \{1000, 2000, 3000\}; \\ \text{PGSE}(20, 500), \end{cases}$$

The corresponding MSDs are 12 μm, 36 μm and 94 μm respectively. The maximum relative difference is about 12% for $\Delta = 5\delta = 5$ ms and drops to 3% for $\Delta = 200\delta = 200$ ms.

5.3. Thick plane

Now we compare signals computed by Method 1, 2, and 3 for the Thick Plane for the following dMRI parameters:

$$\begin{cases} \text{PGSE}(1, 40) \\ \text{PGSE}(1, 200) \end{cases}, \begin{cases} \boldsymbol{u}_g = [1, 0, 0] \\ \boldsymbol{u}_g = \frac{[1,1,1]}{\sqrt{3}} \end{cases}, \quad b = \{1000, 2000, 3000, 4000\};$$

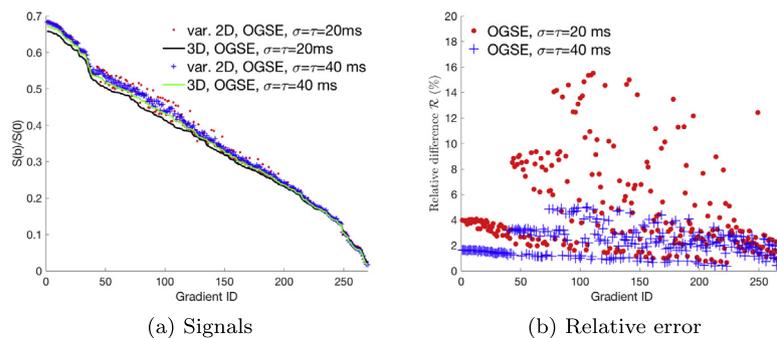
(a) Signals   (b) Relative error

Fig. 9. Signals for cosine OGSE sequences in the variable-thickness tree compared to the reference signals for $\sigma = \tau = 20$ ms and $\sigma = \tau = 40$ ms (b). The approximation gets better at the longer diffusion time. The maximum relative difference is about 5% for $\sigma = \tau = 40$ ms (b).
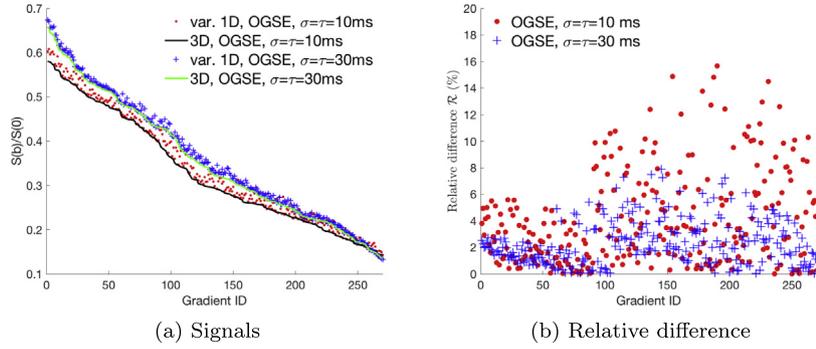
(a) Signals   (b) Relative difference

Fig. 10. Signals for 1D and 3D models of the Neuron for a cosine OGSE sequence with $\sigma = \tau = 10$ ms and $n = 2$ versus 270 gradients distributed in a sphere.
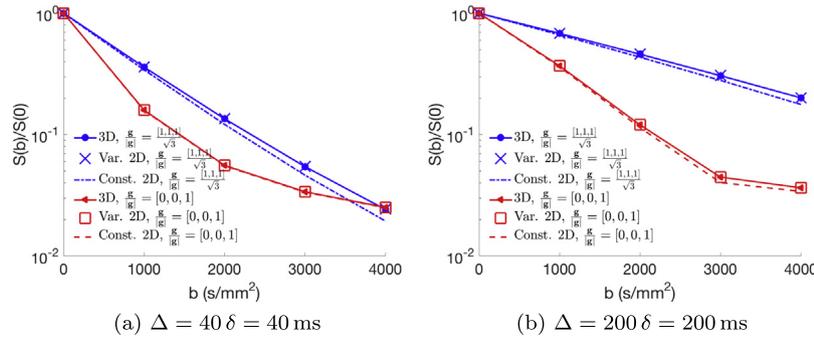

(a) $\Delta = 40\,\delta = 40$ ms   (b) $\Delta = 200\,\delta = 200$ ms

Fig. 11. Computed signals on a thick plane with variable thickness $\eta(x, y, z) = 9/4 - x/10 - z/50$ for $\Delta = 40\,\delta = 40$ ms (a), $\Delta = 200\,\delta = 200$ ms (b) and two gradient directions $\boldsymbol{u}_g = [0, 0, 1]$, $\boldsymbol{u}_g = \frac{[1,1,1]}{\sqrt{3}}$. The variable cross-Section 2D model approximates accurately the full model whereas the constant cross-section model gives a good approximation for $\boldsymbol{u}_g = [0, 0, 1]$ and a less good approximation for $\boldsymbol{u}_g = \frac{[1,1,1]}{\sqrt{3}}$ with around 13% in maximum relative difference.

(a) Signals   (b) Relative difference
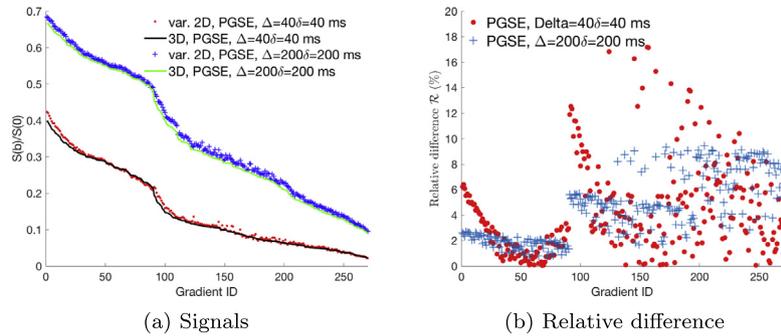
Fig. 12. The simulations were performed for the Model ECS (Fig. 6) with two PGSE sequences $\Delta = 40\,\delta = 40$ ms and $\Delta = 200\,\delta = 200$ ms. The signals in the 2D manifold domain in comparison to the 3D model are shown in (a). The maximum relative difference for $\Delta = 40$ ms is about 17% and decreases to 9% for $\Delta = 200$ ms (b). The large errors only occur for a few gradient directions and the averaged difference over all gradient directions is about 4% for both cases.

The variable cross-section model approximates accurately the full model whereas the constant cross-section model gives good approximations for $\boldsymbol{u}_g = [0, 0, 1]$ but a less accurate approximation for $\boldsymbol{u}_g = \frac{[1,1,1]}{\sqrt{3}}$, with around 13% maximum relative difference (Figs. 11a, b).

5.4. Model ECS

In the last set of simulations, we compare Method 1 and Method 2 for the model ECS. The dMRI parameters are:

$$\begin{cases} \text{PGSE}(1, 40) \\ \text{PGSE}(1, 200), \boldsymbol{u}_g \in \mathcal{G}, \quad b \in \{1000, 2000, 3000\}; \\ \text{PGSE}(1, 500) \end{cases}$$

Fig. 12a shows the signals in the 2D manifold domain in comparison to the 3D model. The maximum relative difference for
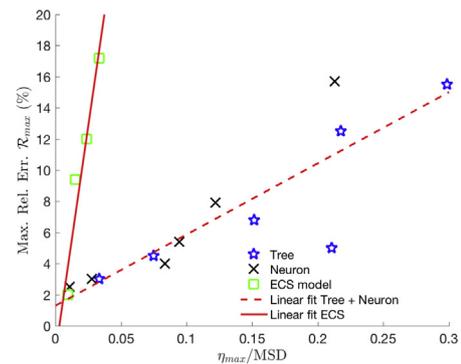

Fig. 13. The relative error $\mathcal{R}$ goes to zero linearly with $\eta_{max}/$MSD.

Table 3
The relative error $\mathcal{R}$ gets smaller as η/MSD gets smaller and a huge speedup is obtained by the manifold model over the full 3D model.

Sample (thickness η)	Sequence ms	t_D ms	MSD μm	$\mathcal{R}_{mean}$ (%)	$\mathcal{R}_{max}$ (%)	Speedup (times)
Tree (0.2–2 μm)	PGSE(1, 5)	4.7	9.2	3.8	12.5	
	PGSE(1, 10)	9.7	13.2	2.5	6.8	> 9000
	PGSE(1, 40)	39.7	26.7	1.0	4.5	
	PGSE(1, 200)	199.7	60	1.0	3.0	
	OGSE(20)	2.5	6.7	4.7	15.5	
	OGSE(40)	5	9.5	2.2	5.0	
Neuron 1 μm	PGSE(5, 10)	8	12	1.0	4.0	> 800
	PGSE(20, 80)	73	36	1.0	3.0	
	PGSE(20, 500)	493	94	1.0	2.5	
	OGSE(10)	1.3	4.7	4.1	15.7	
	OGSE(30)	3.8	8.2	2.3	7.9	
	OGSE(50)	6.3	10.6	1.9	5.4	
ECS (0.3–0.9 μm)	PGSE(1, 40)	40	27	4.3	17.2	> 20
	PGSE(1, 200)	200	60	4.5	9.4	
	PGSE(1, 500)	499.7	94.8	0.5	2.0	

$\Delta = 40$ ms is about 17% and decreases to 9% for $\Delta = 200$ ms (Fig. 12b). However, the large errors only occur for a few gradient directions and the averaged difference over all gradient directions is about 4% for both cases.

6. Discussion

We proposed an efficient finite element discretization for the diffusion MRI simulation of thin layer and thin tube domains that works for general pulse sequences. By transferring the variable thickness to the variational form on a manifold, our proposed approach (Method 2) approximates the full 3D model (Method 1) much better than the previous manifold model [29] with a constant thickness (Method 3). Fig. 8 shows that in some cases, the improvement can be large. In fact, it stands to reason that if the thickness is not uniform, Method 3 does not converges to Method 1 as the effective diffusion time t_D tends to infinity.

Fig. 13 shows the convergence of Method 2 to Method 1 and there is a linear relationship between $\mathcal{R}$ and η_{max}/MSD (the fitting line does not cross the origin exactly due to numerical errors of the finite element solution).

In Table 3 we summarize the accuracy and the computational efficiency of our proposed method (Method 2) compared to the reference method (Method 1). It shows that the computational timing on the manifolds is significantly reduced compared to the full 3D models. The 1D manifolds give the largest benefit since two topological dimensions were removed and it can run thousands of times faster. The improvement of the 2D manifold is less significant but the computation is still 20 times faster.

As discussed in [26], the FEM approach is much more efficient than the Monte-Carlo simulations for the short pulse limit. It is expected that the conclusions comparing FEM with Monte-Carlo simulations apply to the general Bloch-Torrey PDE. Thus, the approach we propose here (Method 2) can be used to replace the Monte-Carlo simulations in [13], especially since the use of one-dimensional components in that study was justified by the long diffusion times. In addition, our approach can also contribute to the extraction of morphological properties of different types of neurons that was preliminarily evoked in [14] using HARDI-type acquisitions. Similarly, extracting information about the ECS using manifold models is an exciting prospect.

This new approach helps to reduce significantly both the computational cost of the solver and the complexity of mesh generation for FEM simulations. For a large number of experiments in this paper, the 3D simulations required the KTH Beskow supercomputer [50] whereas the simulations of the reduced models were still fast on a personal laptop. Interestingly, since the manifold simulations are less memory-demanding and less time-consuming, we could perform them in a free cloud machine, Colab notebooks [51], that requires no setup. It would make the simulation of diffusion MRI very straightforward. This package is available upon request.

In the future, unknown fields defined over domains of different topological dimensions can be coupled as proposed in [52] to simulate more complex geometries.

7. Conclusions

We proposed an efficient finite element discretization for the diffusion MRI simulation of thin layer and thin tube domains. The new method works for general pulse sequences and we found a linear relationship between the accuracy of our method and the ratio between the thickness of the "thin" dimension and the unhindered diffusion distance. Using our formulation, the full 3D simulations are reduced to computations either on one-dimensional manifolds for neurites or on two-dimensional manifolds for the extra-cellular space while maintaining computational accuracy. This approach can be used to investigate the morphological properties of brain cells that are out of reach of existing techniques.

In the future, the proposed discretization can be coupled with full 3D models as mixed-dimensional partial differential equations defined over domains of differing topological dimensions to enable simulations of diffusion MRI on more complicated geometries. The implementation of the method on supercomputers is also an interesting direction.

Appendix A. Implementation in FEniCS

```
v = TestFunction(W)
vr, vi = v[0], v[1]

u = TrialFunction(W);
ur, ui = u[0], u[1]

def FuncF(ft, gnorm, G, ur, ui, vr, vi, D):
    Fr = ft*gnorm*G*ui*vr - D*inner(grad(ur), grad(vr))
    Fi = - ft*gnorm*G*ur*vi - D*inner(grad(ui), grad(vi))
    return Fr + Fi

G=Expression("x[0]*g0+x[1]*g1+x[2]*g2", g0=g0, g1=g1,
    g2=g2,domain=mesh,degree=1)

a = eta*(ur/dt*vr+ui/dt*vi-theta*FuncF(ft, gnorm, G, ur , ui , vr, vi,
    D))*dx

L = eta*(ur_0/dt*vr+ui_0/dt*vi+(1-theta)*FuncF(ft_prev, gnorm, G, ur_0,
    ui_0, vr, vi, D))*dx
```

where `W` is a vector function space defined in FEniCS Python as

```
V = FunctionSpace(mesh,"CG",porder)
W = MixedFunctionSpace([V, V])
```

In C++, the definition is different for different topological dimensions. For 2D manifolds it is

```
domain = Cell("triangle", geometric_dimension=3)
V = FiniteElement("CG", domain, 1)
W = MixedElement([V,V])
```

and for 1D manifolds, it is

```
domain = Cell("interval", geometric_dimension=3)
V = FiniteElement("CG", domain, 1)
W = MixedElement([V,V])
```

`ur_0` and `ui_0` indicate the solutions $u_h^{n,r}, u_h^{n,i}$ from the previous time step and `ur` and `ui` indicate the unknowns $u_h^{n+1,r}, u_h^{n+1,i}$. The initial conditions are `ur_0=1` and `ui_0=0` at $t = 0$.

References

[1] M.E. Moseley, J. Kucharczyk, J. Mintorovitch, Y. Cohen, J. Kurhanewicz, N. Derugin, H. Asgari, D. Norman, Diffusion-weighted mr imaging of acute stroke: correlation with t2- weighted and magnetic susceptibility-enhanced mr imaging in cats, AJNR Am. J. Neuroradiol. 11 (3) (1990) 423–429.

[2] S. Warach, D. Chien, W. Li, M. Ronthal, R.R. Edelman, Fast magnetic resonance diffusion-weighted imaging of acute human stroke, Neurology 42 (9) (1992) 1717.

[3] G. Stuart, N. Spruston, M. Häusser, Dendrites, Oxford University Press, 2007.

[4] Nelson Spruston, Pyramidal neurons: dendritic structure and synaptic integration, Nat. Rev. Neurosci. 9 (3) (2008) 206–221.

[5] Giorgio A. Ascoli, Duncan E. Donohue, Maryam Halavi, Neuromorpho.org: A central resource for neuronal morphologies, J. Neurosci. 27 (35) (2007) 9247–9251.

[6] Eva Syková, Charles Nicholson, Diffusion in brain extracellular space, Physiol. Rev. 88 (4) (2008) 1277–1340.

[7] Charles Nicholson, Eva Sykov, Extracellular space structure revealed by diffusion analysis, Trends Neurosci. 21 (5) (1998) 207–215.

[8] Charles Nicholson, Padideh Kamali-Zare, Lian Tao, Brain extracellular space as a diffusion barrier, Comput. Vis. Sci. 14 (7) (2011) 309–325.

[9] Yaniv Assaf, Tamar Blumenfeld-Katzir, Yossi Yovel, Peter J. Basser, Axcaliber: A method for measuring axon diameter distribution from diffusion MRI, Magn. Reson. Med. 59 (6) (2008) 1347–1354.

[10] Daniel C. Alexander, Penny L. Hubbard, Matt G. Hall, Elizabeth A. Moore, Maurice Ptito, Geoff J.M. Parker, Tim B. Dyrby, Orientationally invariant indices of axon diameter and density from diffusion MRI, NeuroImage 52 (4) (2010) 1374–1389.

[11] Hui Zhang, Torben Schneider, Claudia A. Wheeler-Kingshott, Daniel C. Alexander, Noddi: Practical in vivo neurite orientation dispersion and density imaging of the human brain, NeuroImage 61 (4) (2012) 1000–1016.

[12] Dang Van Nguyen, Denis Grebenkov, Denis Le Bihan, Jing-Rebecca Li, Numerical study of a cylinder model of the diffusion MRI signal for neuronal dendrite trees, J. Magn. Reson. 252 (Supplement C) (2015) 103–113.

[13] Marco Palombo, Clémence Ligneul, Chloé Najac, Juliette Le Douce, Julien Flament, Carole Escartin, Philippe Hantraye, Emmanuel Brouillet, Gilles Bonvento, Julien Valette, New paradigm to assess brain cell morphology by diffusion-weighted mr spectroscopy in vivo, Proc. Natl. Acad. Sci. U S A 113 (24) (2016) 6671–6676, 201504327[PII].

[14] Demian Wassermann, Dang Van Nguyen, Guillermo Gallardo, Jing-Rebecca Li, Weidong Cai, Vinod Menon, Sensing Von Economo Neurons in the Insula with Multi-shell Diffusion MRI, International Society for Magnetic Resonance in Medicine, Poster, 2018.

[15] Charles Nicholson, Diffusion and related transport mechanisms in brain tissue, Rep. Prog. Phys. 64 (7) (2001) 815.

[16] Andrada Ianuș, Daniel C. Alexander, Ivana Drobnjak, Microstructure imaging sequence simulation toolbox, in: Sotirios A. Tsaftaris, Ali Gooya, Alejandro F. Frangi, Jerry L. Prince (Eds.), Simulation and Synthesis in Medical Imaging, Springer International Publishing, Cham, 2016, pp. 34–44.

[17] Ivana Drobnjak, Hui Zhang, Matt G. Hall, Daniel C. Alexander, The matrix formalism for generalised gradients with time-varying orientation in diffusion nmr, J. Magn. Reson. 210 (1) (2011) 151–157.

[18] B.D. Hughes, Random Walks and Random Environments/Barry D. Hughes, Clarendon Press, Oxford, New York, 1995.

[19] Chun-Hung Yeh, Benoît Schmitt, Denis Le Bihan, Jing-Rebecca Li-Schlittgen, Ching-Po Lin, Cyril Poupon, Diffusion microscopist simulator: A general monte carlo simulation system for diffusion magnetic resonance imaging, PLoS One 8 (10) (2013) e76626, PONE-D-13-18755[PII].

[20] M.G. Hall, D.C. Alexander, Convergence and parameter choice for monte-carlo simulations of diffusion MRI, IEEE Trans. Med. Imaging 28 (9) (2009) 1354–1364.

[21] Khieu Van Nguyen, Edwin Hernández-Garzón, Julien Valette, Efficient GPU-based Monte-Carlo simulation of diffusion in real astrocytes reconstructed from confocal microscopy, J. Magn. Reson. 296 (2018) 188–199.

[22] Scott N. Hwang, Chih-Liang Chin, Felix W. Wehrli, David B. Hackney, An image-based finite difference model for simulating restricted diffusion, Magn. Reson. Med. 50 (2) (2003) 373–382.

[23] J. Xu, M.D. Does, J.C. Gore, Numerical study of water diffusion in biological tissues using an improved finite difference method, Phys. Med. Biol. 52 (7) (2007).

[24] Kevin D. Harkins, Jean-Philippe Galons, Timothy W. Secomb, Theodore P. Trouard, Assessment of the effects of cellular tissue properties on ADC measurements by numerical simulation of water diffusion, Magn. Reson. Med. 62 (6) (2009) 1414–1422.

[25] Greg Russell, Kevin D. Harkins, Timothy W. Secomb, Jean-Philippe Galons, Theodore P. Trouard, A finite difference method with periodic boundary conditions for simulations of diffusion-weighted magnetic resonance experiments in tissue, Phys. Med. Biol. 57 (4) (2012) N35.

[26] Benjamin F. Moroney, Timothy Stait-Gardner, Bahman Ghadirian, Nirbhay N. Yadav, William S. Price, numerical analysis of nmr diffusion measurements in the short gradient pulse limit, J. Magn. Reson. 234 (Supplement C) (2013) 165–175.

[27] Dang Van Nguyen, Jing-Rebecca Li, Denis Grebenkov, Denis Le Bihan, A finite elements method to solve the blochtorrey equation applied to diffusion magnetic resonance imaging, J. Comput. Phys. 263 (0) (2014) 283–302.

[28] Leandro Beltrachini, Zeike A. Taylor, Alejandro F. Frangi, A parametric finite element solution of the generalised blochtorrey equation for arbitrary domains, J. Magn. Reson. 259 (2015) 126–134.

[29] Dang Van Nguyen, J.R. Li, D.S. Grebenkov, D. Le Bihan, Modeling the diffusion magnetic resonance imaging signal inside neurons, J. Phys: Conf. Ser. 490 (1) (2014) 012013.

[30] Dang Van Nguyen, Johan Jansson, Johan Homan. A fenics-hpc framework for multi-compartment bloch-torrey models, in: ECCOMAS Congress 2016 – Proceedings of the 7th European Congress on Computational Methods in Applied Sciences and Engineering, vol. 1, 2016, pp. 105–119.

[31] Van-Dang Nguyen, Johan Jansson, Johan Hoffman, Jing-Rebecca Li, A partition of unity finite element method for computational diffusion MRI, J. Comput. Phys. (2018).

[32] J.C. Ford, D.B. Hackney, Numerical model for calculation of apparent diffusion coefficients (ADC) in permeable cylinders–comparison with measured ADC in spinal cord white matter, Magn. Reson. Med. 37 (3) (1997) 387–394.

[33] Anders Logg, Kent-Andre Mardal, Garth N. Wells, Automated Solution of Differential Equations by the Finite Element Method: the FEniCS Book, Springer Verlag, 2012, XIII, 723 s.: ill.

[34] FEniCS project, http://www.fenicsproject.org, 2003.

[35] M.E. Rognes, D.A. Ham, C.J. Cotter, A.T.T. McRae, Automating the solution of PDEs on the sphere and other manifolds in FEniCS 1.2, Geosci. Model Dev. 6 (6) (2013) 2099–2119.

[36] Erik Burman, Susanne Claus, Peter Hansbo, Mats G. Larson, Andr Massing, Cutfem: Discretizing geometry and partial differential equations, Int. J. Num. Methods Eng. 104 (7) (2015) 472–501.

[37] H.C. Torrey, Bloch equations with diffusion terms, Phys. Rev. Online Archive (Prola) 104 (3) (1956) 563–565.

[38] E.O. Stejskal, J.E. Tanner, Spin diffusion measurements: Spin echoes in the presence of a time-dependent field gradient, J. Chem. Phys. 42 (1) (1965) 288–292.

[39] Mark D. Does, Edward C. Parsons, John C. Gore, Oscillating gradient measurements of water diffusion in normal and globally ischemic rat brain, Magn. Reson. Med. 49 (2) (2003) 206–215.

[40] Paul Callaghan, A simple matrix formalism for spin echo analysis of restricted diffusion under generalized gradient waveforms, J. Magn. Reson. 129 (1) (1997) 74–84.

[41] S. Nicholas Barton, David A. Ham, Complex-valued pde support in ufl and firedrake, https://youtu.be/mNTFtQW359A.

[42] Neuromorpho.org, http://neuromorpho.org/neuron_info.jsp?neuron_name=fru-M-100383.

[43] Open cascade. salome: The open source integration platform for numerical simulation, http://www.salome-platform.org.

[44] Beta cae systems, ansa pre-processor: The advanced cae pre-processing software for complete model build up, https://www.beta-cae.com.

[45] Mark C. DeLano, Thomas G. Cooper, James E. Siebert, Michael J. Potchen, Karthik Kuppusamy, High-b-value diffusion-weighted mr imaging of adult brain: Image contrast and apparent diffusion coefficient map features, Am. J. Neuroradiol. 21 (10) (2000) 1830–1836.

[46] Benjamin A. Hoff, Thomas L. Chenevert, Mahaveer S. Bhojani, Thomas C. Kwee, Alnawaz Rehemtulla, Denis Le Bihan, Brian D. Ross, Craig J. Galbán, Assessment of multi-exponential diffusion features as MRI cancer therapy response metrics, Magn. Reson. Med. 64 (5) (2010) 1499–1509, 20860004[pmid].

[47] Ariel Rokem, Jason D. Yeatman, Franco Pestilli, Kendrick N. Kay, Aviv Mezer, Stefan van der Walt, Brian A. Wandell, Evaluating the accuracy of diffusion MRI models in white matter, PLoS One 10 (4) (2015) e0123272, 25879933[pmid].

[48] Corey A. Baron, Christian Beaulieu, Oscillating gradient spin-echo (OGSE) diffusion tensor imaging of the human brain, Magn. Reson. Med. 72 (3) (2014) 726–736.

[49] FEniCS-HPC, http://www.fenics-hpc.org/.

[50] KTH Beskow supercomputer, https://www.pdc.kth.se/hpc-services/computing-systems/beskow-1.737436.

[51] Google Colaboratory, https://colab.research.google.com.

[52] J.J. Lee, E. Piersanti, K.-A. Mardal, M.E. Rognes, A mixed finite element method for nearly incompressible multiple-network poroelasticity, ArXiv e-prints, April 2018.